Al–Mg–Zn–(Cu) Crossover Alloy for Powder Bed Fusion–Laser Beam/Metal: Processing–Microstructure–Property Relationships

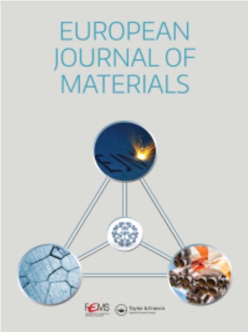

European Journal of Materials

ISSN: 2688-9277 (Online) Journal homepage: www.tandfonline.com/journals/tems20

Al–Mg–Zn–(Cu) Crossover Alloy for Powder Bed Fusion – Laser Beam/Metal: Processing–Microstructure–Property Relationships

Andreas Weidinger , Dmitri Riabov , Sebastian Samberger , Phillip Dumitraschkewitz , Irmgard Weißensteiner , Florian Schmid , Lukas Stemper , Matheus A. Tunes , Lars Nyborg & Stefan Pogatscher

EUROPEAN JOURNAL OF MATERIALS
2026, VOL. 6, NO. 1, 2718638
https://doi.org/10.1080/26889277.2026.2718638

Taylor & Francis by informa

PROCESSING

OPEN ACCESS Check for updates

Al–Mg–Zn–(Cu) Crossover Alloy for Powder Bed Fusion – Laser Beam/Metal: Processing–Microstructure–Property Relationships

Andreas Weidinger[a], Dmitri Riabov[b], Sebastian Samberger[c,d], Phillip Dumitraschkewitz[c], Irmgard Weißensteiner[d], Florian Schmid[e], Lukas Stemper[e], Matheus A. Tunes[c], Lars Nyborg[b] and Stefan Pogatscher[c]

[a]Christian Doppler Laboratory for Advanced Aluminium Alloys, Chair of Nonferrous Metallurgy, Montanuniversitaet Leoben, Leoben, Austria; [b]Industrial and Materials Science, Chalmers University of Technology, Göteborg, Sweden; [c]Chair of Nonferrous Metallurgy, Montanuniversität Leoben, Leoben, Austria; [d]Christian Doppler Laboratory for Deformation - Precipitation Interactions in Aluminium Alloys, Chair of Nonferrous Metallurgy, Montanuniversität Leoben, Leoben, Austria; [e]AMAG Rolling GmbH, Ranshofen, Austria

ABSTRACT
Additive manufacturing expands the processing space for aluminium alloys beyond conventional routes. Emerging Al–Mg–Zn–(Cu) alloys depict a promising alternative for automotive and aviation applications. In addition to that, the exceptional irradiation stability of T-phase precipitates makes them particularly attractive for application in space environments. In this context, AM-enabled repair and refurbishment offer a compelling pathway to restore component performance. We evaluate PBF-LB/M using powder from the commercial AMAG CrossAlloy® .57. The wrought alloy was inert-gas atomized and a portion was post-blended with 0.9 wt.% Fe. Screening 55 parameter sets defined the process window, subsequently refined to two conditions showing relative densities above 98.5%. Processing-induced Mg and Zn evaporation reduced solute content and increased the Mg/Zn ratio. Electron microscopy revealed columnar grains and coarse Mg–Zn–Al–(Cu)-rich precipitates showing morphologies not previously observed in conventionally processed crossover alloys. As-built tensile tests showed UTS ≈ 200 MPa with <1% elongation, and age-hardening variations confirmed limited hardening, with maximum hardness ≈ 120 HBW. The mechanical behaviour is rationalized by a reduced precipitation potential, quantified via thermochemical calculations, and by the defect structure. Based on the results we propose future design strategies for AM-tailored chemistries as a foundation towards future repair applications of crossover alloy components.

IMPACT STATEMENT
This work demonsatrates that the alloy concept can be transferred to additive manufacturing, and identifies the adjustments needed to retain its property advantages in printed components.

ARTICLE HISTORY
Received 13 May 2026
Revised 1 July 2026
Accepted 11 August 2026

KEYWORDS
Al–Mg–Zn alloys; additive manufacturing; crossover alloys; electron microscopy; PBF-LB/M

1. Introduction

Aluminium alloys produced by Powder Bed Fusion – Laser Beam/Metal (PBF-LB/M) have gained increasing attention due to their potential for lightweight structural applications and their suitability for complex geometries that cannot be manufactured by conventional routes (DebRoy et al., 2018; Hoffmann & Elwany, 2023). Moreover, PBF-LB/M has potential for the repair and refurbishment of aluminium alloys, as it enables highly localized material deposition with precise geometrical control and tailored microstructures beyond the limits of conventional repair routes (DebRoy et al., 2018). In general, additive manufacturing (AM) is of strategic importance for space applications, as it allows on-demand fabrication and in-situ repair under extreme environments, thereby reducing launch mass, logistics complexity, and dependence on Earth-based supply chains (Hoffmann & Elwany, 2023; Tunes, 2026).

Despite this potential, the processability of some wrought aluminium alloy systems remains limited in PBF-LB/M because of several factors, not exhaustively: a wide solidification range, high suscepti-

CONTACT Andreas Weidinger andreas.weidinger@unileoben.ac.at Christian Doppler Laboratory for Advanced Aluminum Alloys, Chair of Nonferrous Metallurgy, Montanuniversitaet Leoben, Franz-Josef Straße 18, 8700 Leoben, Austria.

bility to hot cracking, and significant evaporation of alloying elements under laser melting (DebRoy et al., 2018; Herzog et al., 2016). These challenges restrict the use of e.g., high strength 7xxx series alloy systems, even though they would offer a favourable combination of properties achieved via precipitation hardening in conventionally processed conditions (J. H. Martin et al., 2017; Rometsch et al., 2022).

Among the wrought aluminium alloy families, a novel class based on the Al–Mg–Zn system, the Al–Mg–Zn-(Cu) crossover alloys are of increasing interest because of the formation of the compositionally complex T-phase ($Mg_{32}(Al,Cu)_{49}$) precipitates (Cao et al., 2017). These precipitates have been reported to have a high ability to function as sinks for point defects in environments where irradiation damage, such as for deep space missions, is relevant (Cao et al., 2017; Stemper et al., 2021; Tunes et al., 2020; Willenshofer et al., 2023, 2026). T-phase precipitates typically develop in commercial wrought alloy manufacturing during slow cooling or controlled ageing treatments (Stemper et al., 2021). The formation of these under rapid thermal cycling in PBF-LB/M has not yet been systematically studied, and to the best of our knowledge, Al–Mg–Zn–(Cu) crossover alloys have not yet been produced using this processing method. However, the extremely high solidification rates, steep thermal gradients, repeated layer wise reheating (Yoshioka & Eshraghi, 2023), and vacancy supersaturation characteristic of the process is known to promote non-equilibrium precipitation and coarsening mechanisms (Qin et al., 2020). Understanding how these mechanisms influence T-phase formation and distribution is therefore essential for extending the application of this alloy system to additive manufacturing.

A central challenge in alloys containing Mg and Zn within the method of PBF-LB/M is the metal evaporation, induced by high vapour pressures at laser melt pool temperatures (Knacke & Stranski, 1956; Stranski & Nesmeyanov 1963). This leads to measurable compositional shifts between powder and as-built material, typically increasing the Mg to Zn ratio and reducing the overall solute content available for precipitation hardening (Babu et al., 2020; Knacke & Stranski, 1956; Zhou et al., 2020). These effects have been described for various Al–Mg and Al–Zn alloys, but quantitative studies for crossover compositions containing both elements in combination with Cu are yet scarce (Babu et al., 2020; Klein et al., 2023), demanding further studies.

In addition to solute evaporation, the process window of 7xxx alloys within methods of additive manufacturing (AM) is inherently narrow. At insufficient energy input, incomplete melting promotes lack of fusion porosity, while excessive energy input increases melt pool depth and solidification stresses, which enhances hot cracking (Casati et al., 2019; T. Wang et al., 2022). Process parameters that balance these competing mechanisms are therefore essential for achieving dense components with acceptable microstructural integrity. Both volumetric energy density (VED) and line energy density (LED) have been identified as relevant descriptors for melt pool stability and defect formation in aluminium alloys and other crack sensitive systems like Ni-base superalloys (Fardan et al., 2024; Ferro et al., 2020; Zhou et al., 2020).

The aim of this work is to establish a relationship between processing parameters, solute evaporation, T-phase formation, and mechanical properties in a commercial AMAG CrossAlloy® .57 alloys processed by PBF-LB/M, to evaluate their potential for the potential repair of such components and the general usability in by PBF-LB/M. A key focus is placed on quantifying Mg and Zn losses and characterizing the formation of non-equilibrium T-phase precipitates in the as-built state and the effects of defects on mechanical performance. Finally, the study proposes crossover alloy design and processing strategies to enhance compatibility and performance in PBF-LB/M.

2. Experimental methods

2.1. Powder production

The pre-alloyed spherical powder used in this study was directly manufactured from a commercial wrought AMAG CrossAlloy® .57, provided by the company AMAG rolling GmbH, using Vacuum Induction Melting Inert Gas Atomization (VIGA) technology, yielding a particle size distribution ranging from 20 to 63 µm. The atomization process was conducted on a machine from ALD Vacuum Technologies within the temperature range of 750–800 °C.

The powder (.57) contains 4.51 wt.% Mg, 3.53 wt.% Zn, 0.50 wt.% Cu, 0.07 wt.% Fe, 0.04 wt.% Si, and 0.39 wt.% Mn (balance Al), corresponding to an Mg/Zn ratio of 1.28. A portion of the base powder was subsequently blended in a roller mixer for 24 h with an addition of 0.83 wt.% Fe powder (average particle size ~10 µm), increasing the total iron content to 0.9 wt.% in the modified composition (.57 + Fe). This alloy modification aimed at a further evaluation of compositional sensitivity, in line with prior reports highlighting the role of Fe in promoting dispersoid formation and influencing cracking susceptibility (Chen et al., 2021; Fardan et al., 2024).

The cumulative particle size distribution of the powder was determined via liquid optical particle size measurement with a Litesizer DIA. For Powder .57 the d_{10}, d_{50} and d_{90} were measured to 21.3 µm, 39.7 µm and 70.7 µm. For Powder .57 + Fe the d_{10}, d_{50} and d_{90} were measured to 21.7 µm, 42.0 µm and 81.9 µm. This is consistent with a typical powder used in PBF-LB/M-process (Beevers et al., 2024).

Figure 1 shows the highly spherical-shape of the powder in the original stage (A) and with 0.9 wt.% iron (B) as observed by Scanning Electron Microscopy (SEM) and Energy Dispersive X-ray (EDX) spectroscopy mapping.

2.2. PBF-LB/M-process

The printed samples were produced at the Institute of Materials Science at Chalmers University of Technology in Sweden. A standard EOS M290 (Electro Optical Systems GmbH, Germany) system was used for the printing process. This machine is equipped with a Yb fibre laser featuring a nominal power of 370 W and a focused beam diameter of ~90 µm. All tested specimens were built on a building platform heated to 110 °C under a constant argon flow to reach a remaining oxygen content below 0.1% in the process chamber and prevent oxidation during melting.

- ***Volume Energy Density (VED)***

Density is a critical factor influencing the performance of parts produced by PBF-LB/M. The VED is widely recognized as a key parameter for assessing the impact of engineering variables on the

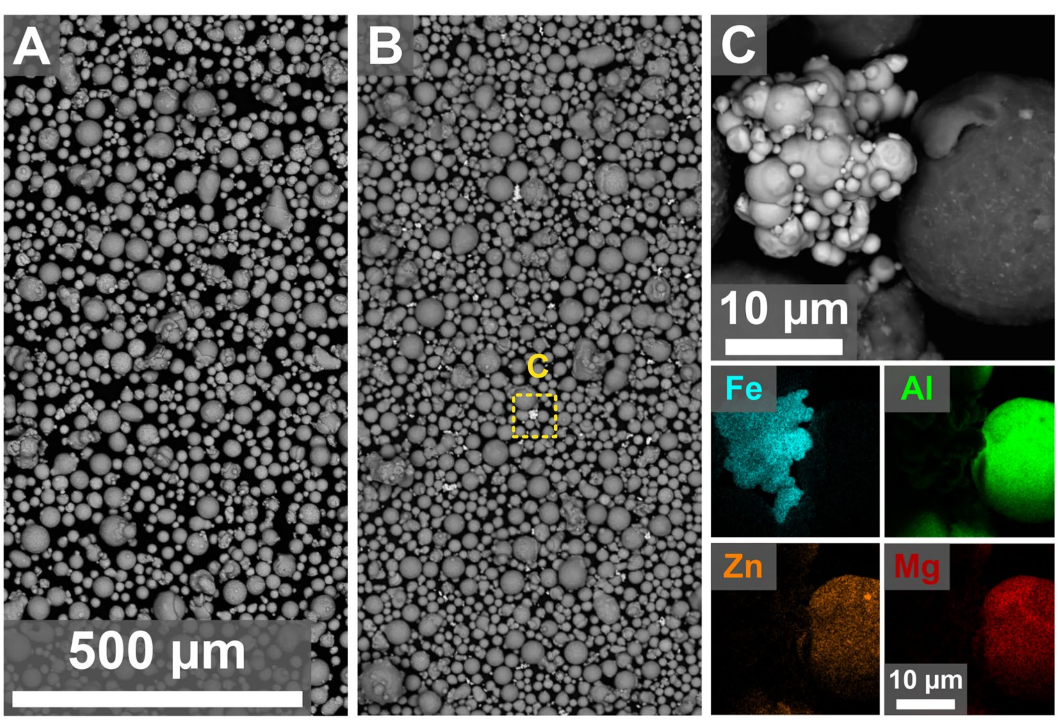

Figure 1. Scanning electron microscopy (SEM) images of the investigated feedstock powders: (A) original Al–Mg–Zn–(Cu) crossover alloy powder; (B) blended Al–Mg–Zn–(Cu) powder with Fe addition; and (C) detail of an individual Fe particle with corresponding EDX elemental maps (Fe, Al, Zn, Mg).

quality of manufactured components (Zhou et al., 2020). Equation (1) can be used to calculate the parameter in (J/mm³).

$$VED\left[{}^{J}\!/_{mm^3}\right] = \frac{P[W]}{v\left[{}^{mm}\!/_{s}\right]\cdot h[mm]\cdot t[mm]} \tag{1}$$

P represents the laser power (W), v denotes the scanning speed in (mm/s), h indicates the hatch spacing (mm), and t refers to the nominal powder layer thickness also in (mm).

- ***Line Energy Density (LED)***

In addition, the LED shown by Equation (2) is considered as a key parameter to control melt pool morphology (Fardan et al., 2024).

$$\boldsymbol{LED}\left[{}^{J}\!/_{mm}\right] = \frac{\boldsymbol{P}[\boldsymbol{W}]}{\boldsymbol{v}\left[{}^{mm}\!/_{s}\right]} \tag{2}$$

For the present study, laser power (P) was varied between 150 and 370 W, while scan speeds ranged from 900 to 5000 mm/s. The layer thickness was held constant at 30 µm and with a hatch distance between 0.025 and 0.19 mm. This parameter space provided LED values in the range of approximately 0.075–0.410 J/mm, enabling a systematic evaluation of its influence on cracking, porosity, and microstructural development.

All process window optimization experiments were performed printing cubic specimens with an edge length of 10 × 10 × 10 mm. Only the final parameter sets, for mechanical testing, were produced as rectangular blocks (10 × 15 × 80 mm) and machined into tensile specimens according to EN ISO 6892–1 with an M10 threaded head (Form B) (Aegerter et al., 2011).

2.3. Parameter space evaluation

We utilized a multi-stage design of experiments (DOE) to systematically determine optimal and stable process conditions. Building upon an initial screening study that established the fundamental process window of the material (Weidinger et al., 2025), the present work refined and optimized the parameter space in a structured manner.

In the initial stage, 55 parameter sets with focus on volumetric energy density (VED) were screened (see Appendix for details) (Fardan et al., 2024; Ferro et al., 2020). Based on this wide screening, the study was refined to final parameter sets (see Table 2) emphasizing LED, which provides a more direct measure of melt track stability (Fardan et al., 2024). From this iterative DOE process, two final parameter sets were identified, corresponding to a VED of 70 J/mm³ combined with LED values of 0.125 (#6) and 0.150 J/mm (#7).

2.4. Characterization

Specimens were divided along the build direction and subsequently mounted on MultiFast resin (Struers). Starting by grinding and polishing with 200- and 500-micron silica discs and followed by three polishing steps. Beginning with 9 µm to 3 µm down to the final step with 1 µm diamond based polishing fluid. All specimens were prepared on a Abrapol-2 machine.

Optical microscopy was performed using a Zeiss AXIOSCOPE 7 (OME) combined with the stacking software from Zeiss ZEN core v 2.7. Porosity measurements were conducted using ImageJ software, where defects were defined as the ratio of the total area occupied by pores to the overall measurement area of the sample. In addition, to make all areas of lower density visible, the threshold for all images was set to 0–80 grey values. The circularity value was set to 0.3–1.0.

To make the solidification morphology and melt pool depth visible, the specimens were swab etched using Kroll's reagent (Vander Voort, 1999). Melt pool geometries were evaluated via light optical microscopy, of the top processed layer. The melt pool width and depth were quantified using ImageJ software. For each individual melt pool, three independent measurements were performed for both width and depth, and the corresponding mean values were calculated.

Electron microscopy of the powder and printed material as well as fracture surface analysis was performed using a JEOL 7200 F FEG-SEM field emission gun scanning electron microscope, equipped with a Symmetry S2 Electron Backscatter Diffraction (EBSD) detector and an EDX detector (XMax-100, Oxford Instruments). EBSD measurements were performed at an accelerating voltage of 20 kV and a working distance of 16 mm, using a specimen holder with a 70° pre-tilt. Grain reconstruction was performed with a misorientation tolerance of 5°, in accordance with ASTM E2627–13 (ASTM International 2019). To improve data quality, the "auto smoothing" function of the Oxford Instruments AZtec software (Oxford Instruments 2022) was applied, which removes isolated pixels (wild spikes) and iteratively eliminates zero solutions. All EBSD measurements for grain size analysis were conducted at identical magnification to ensure directly comparable, non-normalized data sets.

Transmission electron microscopy was performed using a Thermo Fisher Scientific Talos F200X scanning transmission electron microscope. For statistical analyses, high-angle annular dark-field (HAADF) imaging, bright-field transmission electron microscopy (BF-TEM), and energy-dispersive X-ray spectroscopy (EDX) were employed. Specimens prepared for SEM analysis were subsequently used for site-specific transmission electron microscopy sample preparation. Electron-transparent lamellae were extracted from selected regions using focused ion beam (FIB) milling and lift-out techniques. Final thinning was performed at low ion beam currents to minimize ion-induced damage.

2.5. Heat treatment and mechanical testing

Two different heat treatment strategies were investigated. Both approaches, start by homogenizing the samples at 465 °C for 4 h, followed by a rapid quenching via water. The first approach of a two-stage ageing treatment consisted of an initial stage at 100 °C for 5 h, followed by a second stage at 180 °C with a holding time of 0 to 10 h. The treatment is denoted HT1. In the second heat treatment approach (denoted HT2), homogenization was followed by a first ageing stage at 80 °C for 18 h, promoting the formation of solute clusters that serve as nucleation precursors for subsequent precipitation during the second ageing stage (Stemper et al., 2021). Based on prior studies, the second ageing step was selected at 130 °C for up to 110 h, since prolonged ageing at low temperature promotes the formation of ultrafine clusters and precipitates while suppressing coarsening (Aster et al., 2025). All hardness measurements were conducted using an EMCO-TEST M4 instrument using the Brinell hardening measurement method (HBW 2.5/62.5), with values representing the average of five independent measurements.

Tensile testing was also performed on both as-printed samples and samples subjected to heat treatment, with and without Fe addition. Tensile properties were evaluated using a Zwick/Roell BT1-FR100THW. A2K testing machine equipped with a 50 kN load cell. Three samples were tested in each condition.

3. Results & discussion

3.1. Element loss

A measurable loss of the alloying elements Mg and Zn was observed after processing at different VED values, as summarized in Table 1. The loss increases systematically with higher VED, Zn exhibiting a more pronounced reduction than Mg, consistent with its higher vapour pressure (Knacke & Stranski, 1956). Consequently, both Mg and Zn contents decrease relative to the delivered condition, resulting in a progressive shift of the Mg/Zn ratio. The compositions were determined by ICP-OES in accordance with EN 14242 (ASTM International 2017).

3.2. Thermodynamic simulations

Thermodynamic calculations were performed to estimate the nature and amount of the T-phases occurring as shown in Figure 2. Equilibrium calculations were done using FactSage (Bale et al., 2002) with the FTlight databases and a temperature step size of 5 °C.

Table 1. Mg and Zn content (wt.%), relative losses (Δ%) and resulting Mg/Zn ratios of the .57 alloy in the delivered powder state and after PBF-LB/M processing at different VED values.

Alloy/parameter		Mg [wt.%]	Δ Mg [%]	Zn [wt.%]	Δ Zn [%]	Mg/Zn
.57	Delivered powder	4.51	–	3.53	–	1.28
.57	VED 46 J/mm^3	4.29	−4.7	3.12	−10.9	1.38
.57	VED 70 J/mm^3	3.90	−13.3	2.77	−20.9	1.41
.57	VED 100 J/mm^3	3.85	−14.4	2.68	−23.4	1.44
.57	VED 154 J/mm^3	3.80	−15.6	2.68	−23.4	1.42

Table 2. Overview of the selected parameter sets for further investigation.

Set	Power [W]	Layer [µm]	Temp. [°C]	Speed [mm/s]	Hatch [µm]	VED [J/mm^3]	LED [J/mm]
#1	370	30	110	5000	25	100	0.075
#2	370	30	110	3700	33	100	0.100
#3	370	30	110	2960	42	100	0.125
#4	370	30	110	2467	50	100	0.150
#5	370	30	110	1200	100	100	0.300
#6	350	30	110	2800	60	70	0.125
#7	350	30	110	2333	71	70	0.150

Note: Laser power, layer height, platform temperature, scanning speed and the hatch distance were chosen, the VED, LED and additionally the built-up volume were calculated based on the input parameters.

The simulations indicate the presence of T-phase and show that its fraction is composition-dependent. For the as-printed chemistry VED 70 and 100 J/mm^3 from Table 1 were representatively chosen for the calculation, showing that the achievable T-phase fraction is significantly lower than in the delivered condition.

3.3. Melt pool formation

Figure 3 illustrates the evolution of the melt pool geometry as a function of hatch distance on parameters extracted from the 55 samples from the DOE to fit the matrix. Melt pool boundaries are revealed by Kroll etching, which provides sufficient contrast (Murr, 2018).

With increasing hatch spacing, a continuous widening of the melt pool is observed, with the average width increasing from approximately 136 to 305 µm. In parallel, increasing LED results in a pronounced increase in melt pool depth, from about 104 µm at low energy input to nearly 260 µm at the highest LED. The micrographs reveal that higher energy input not only enlarges the melt pool dimensions but also alters the degree of remelting between next tracks, leading to distinct overlap morphologies. At intermediate hatch distances, partial overlap between neighbouring melt-tracks enables localized remelting of already solidified material, which can locally reduce thermal stress and partially heal micro-cracks, as evidenced by interrupted or blunted crack paths. These observations highlight the competing effects of energy input and track overlap. Excessive melt pool depth increases crack driving forces. Nevertheless, controlled remelting at intermediate hatch spacing can mitigate crack propagation through microstructural homogenization and stress redistribution.

3.4. Process window optimization

The processing of alloy .57 and .57 + Fe required a systematic exploration within the parameter space to find a stable process window. Taking all 55 tested parameter sets into consideration, only a limited range ensured sufficient density and reproducibility. Stable processing was achieved at VED values between 70 and 100 J/mm^3, laser power of 350–370 W, a platform preheating of 110 °C, and a constant layer height of 30 µm.

The parameter sets selected for further investigation (Table 2) were chosen to maintain comparable VED levels while systematically varying LED through adjustments in scan speed and hatch distance. This strategy enables targeted modification of the melt pool geometry, particularly melt pool depth (as visible in Figure 6), which has been proven in previous works to strongly influence solidification behaviour and crack sensitivity in alloys with limited printability (Fardan et al., 2024).

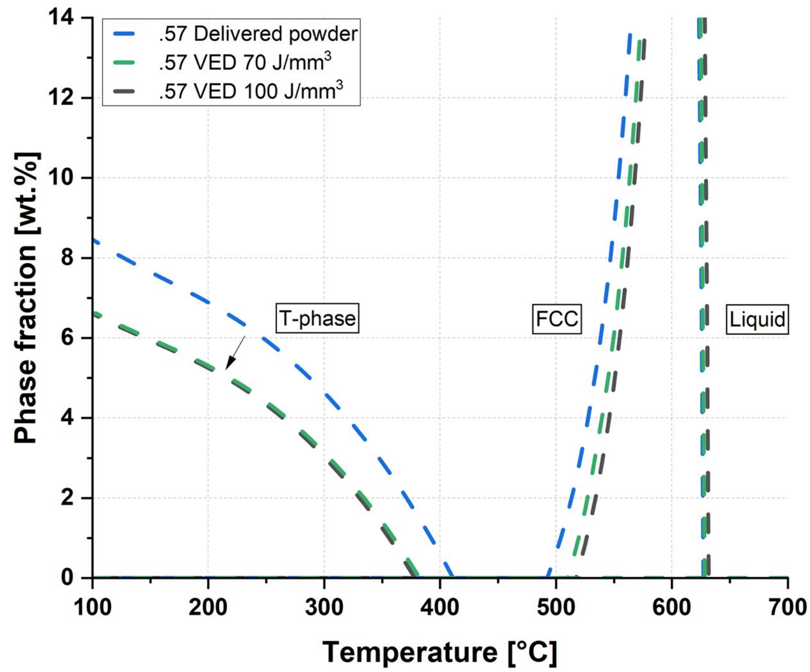

Figure 2. Phase evolution during thermal processing: an overview of FactSage-predicted phase fractions as a function of temperature for the different alloy compositions.

3.5. Defect morphology

Porosity was determined as described in Section 2.4. Figure 4 provides a comparative measure of defects for each parameter set out of Table 2. The increase in melt pool depth with rising LED is accompanied by a clear increase in crack density, most notably visible for parameter set #5 in Figure 4. In crack-sensitive alloys, deeper melt pools, and therefore, steeper thermal gradients generate higher solidification shrinkage stresses during the final stages of solidification. This behaviour is consistent with literature reports linking excessive melt pool penetration and keyhole-adjacent melting regimes to increased crack susceptibility, e.g., in aluminium- or nickel-based alloys (Fardan et al., 2024; Stopyra et al., 2020).

At low LED (0.075–0.100 J/mm), the samples exhibited incomplete melting and lack-of-fusion defects. In contrast, at higher values (≥0.200 J/mm), hot cracking became dominant.

Based on these findings, the final specimens were produced at VED of 70 J/mm³ with LED values of 0.125 and 0.150 J/mm (Table 2, #6 and #7). The reduced VED also minimizes Mg and Zn evaporation losses (Table 1). For vertically, VED was lowered further to prevent overheating at specimen corners. All analyses were conducted on specimens from conditions #6 and #7. Although relative densities above 98.5% were achieved, residual defects remain and are shown to govern mechanical performance in Chapter 3.8.

3.6. Grain structure

Electron backscatter diffraction orientation maps of the as-printed specimens reveal a pronounced anisotropic grain morphology for both parameter sets visible in Figure 5. In cross-sections perpendicular to the build direction (BD), the microstructure is dominated by relatively equiaxed and rounded grains with a heterogeneous orientation distribution. In contrast, sections taken parallel to the BD exhibit strongly elongated, columnar grains extending over several hundred micrometres. This behaviour is explained by epitaxial growth over several layers and commonly found in PBF-LB/M (Schimbäck et al., 2022).

In comparison, #7 samples exhibit a slightly more pronounced grain elongation along the build direction than #6, indicating a higher degree of directional solidification and epitaxial grain growth. The addition of iron does not fundamentally alter the overall grain morphology (see Figure 5 .57 + Fe).

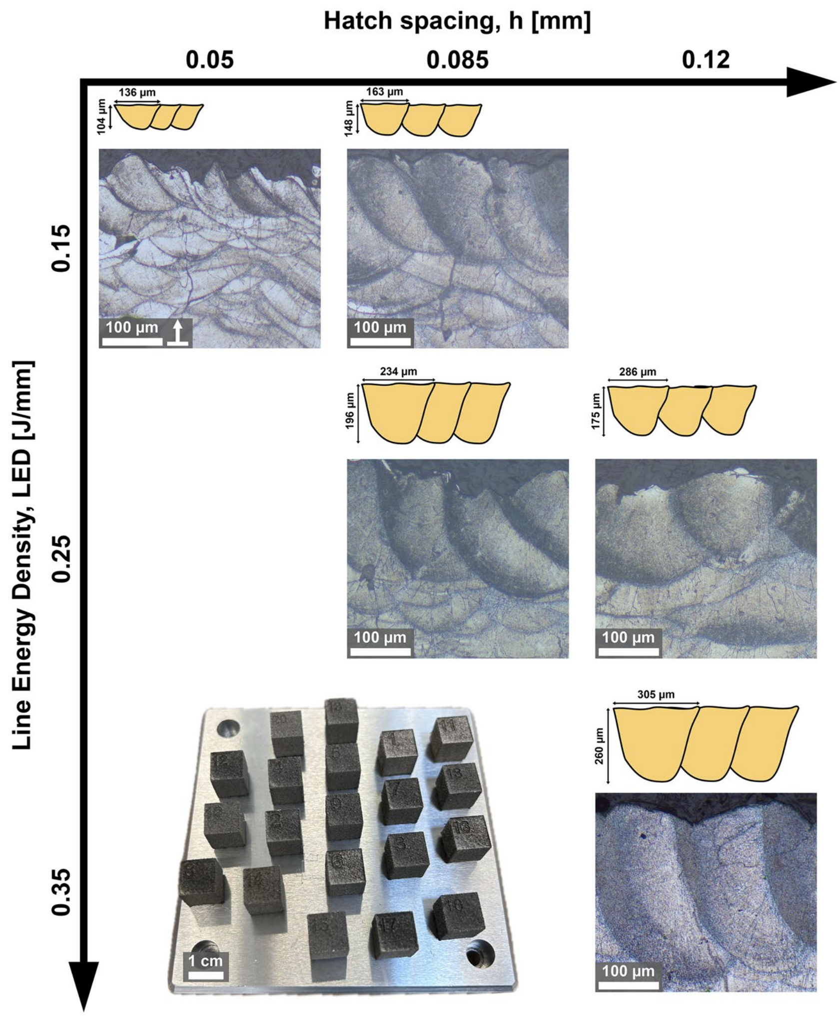

Figure 3. Melt pool cross-sections revealed by Kroll etching showing the influence of hatch distance and line energy density (LED) on melt Pool geometry and crack formation.

Nevertheless, the dominant feature across all conditions remains the presence of long, uninterrupted columnar grains aligned with the heat flow direction.

The observed grain morphology parallel to the build direction was reported to be unfavourable regarding crack resistance (Mair et al., 2022). Cracks propagating parallel to the BD encounter only limited grain boundary deflection and experience minimal crystallographic barriers, enabling rapid and stable crack growth along preferential paths (DebRoy et al., 2018; Samberger et al., 2023).

3.7. Precipitate microstructure

Scanning transmission electron microscopy (S/TEM) combined with EDX mapping was performed on materials in the as-printed stage (.57, #7). Two characteristic features are observed: (i) large, nearly spherical particles and (ii) significantly finer precipitates in their vicinity.

The coarse particles, several hundred nanometres in diameter, show strong enrichment in Zn, Mg and Cu, consistent with a Mg–Zn–Al–(Cu)-rich phase related to the T- or η-phase family, or potentially a non-equilibrium variant not previously described (Stemper et al., 2022). Fe-rich dispersoids are frequently present in their centre, suggesting preferential sites for heterogeneous nucleation. These results are shown in Figure 6. Such coarse precipitate morphologies have not been reported in conventionally processed crossover alloys (Klein et al., 2021; Stemper et al., 2022). According to the calculated solvus temperatures in Figure 2, this phase is not expected to solidify directly from the melt under equilibrium conditions. Their formation is attributed to solid-state decomposition of a

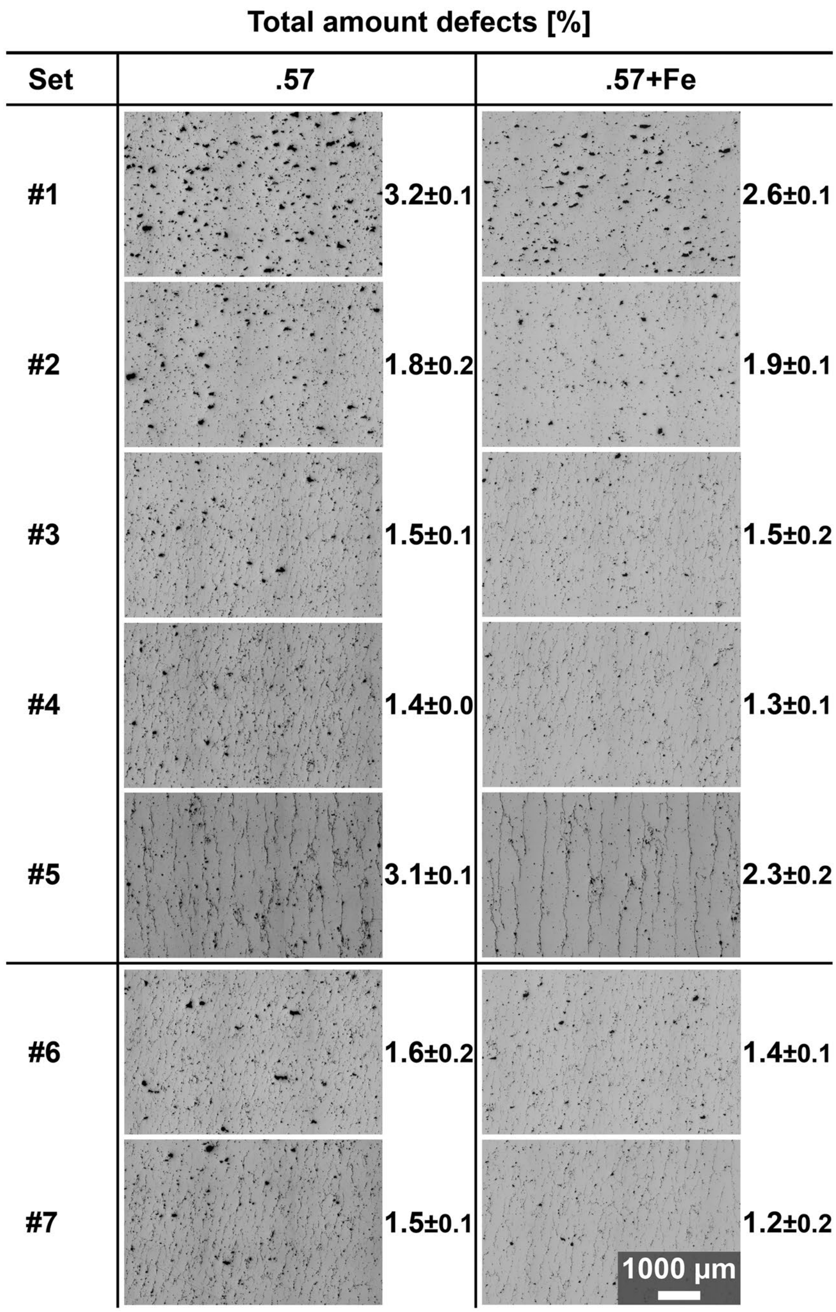

Figure 4. Structural integrity of the printed samples as presented in Table 2.

supersaturated Al matrix during the cyclic sub-solvus thermal excursions of layer-by-layer deposition (Aster et al., 2025; Samberger et al., 2023; Stemper et al., 2021).

Surrounding the coarse particles, a second population of nanoscale precipitates (tens of nanometres) is observed at higher magnification. As shown in Figure 7, these are enriched in Zn and Mg but show no detectable Cu enrichment. Spectral phase mapping of the EDX data suggests both populations share a similar compositional signature, potentially belonging to the same Mg–Zn–Al-rich phase family. Their formation is rationalized by heterogeneous nucleation at geometrically necessary dislocations, which provide favourable nucleation sites despite locally reduced matrix supersaturation (Aster et al., 2025; Samberger et al., 2023; Stemper et al., 2021).

Such dislocations may originate from quench stresses caused by thermal expansion mismatch between the observed coarse Mg–Zn–Al-rich phase and α-Al, as described in Ebenberger et al. (2019). In addition, the cyclic thermal exposure during layer-by-layer deposition and platform heating

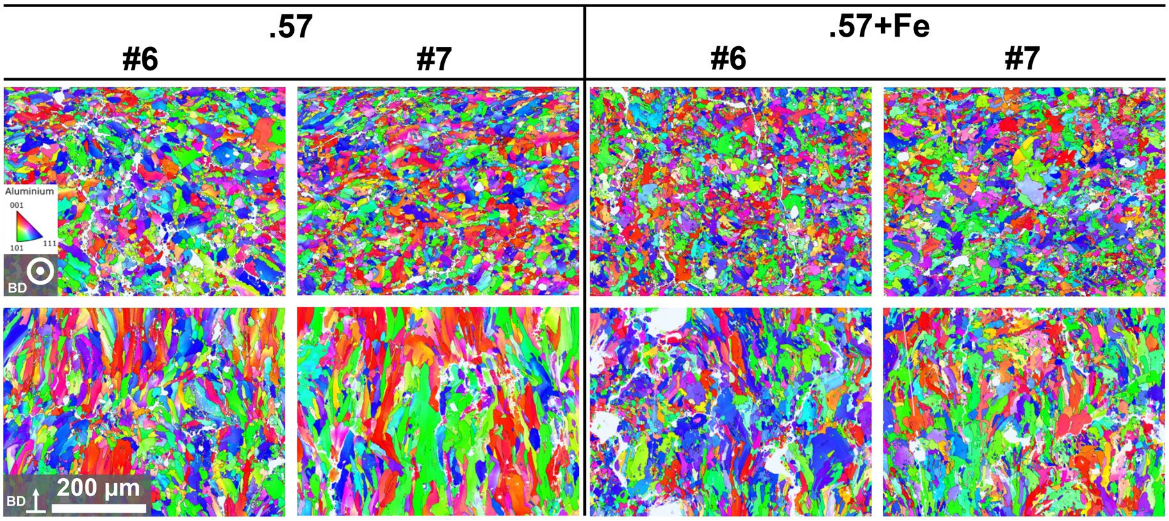

Figure 5. SEM investigation via EBSD orientation maps of the printed specimens of the alloys .57 and .57 + Fe with the print parameters according to Table 2 in the as-printed condition. The top row shows cross-sections perpendicular to the build direction (BD), while the bottom row presents sections parallel to the BD.

promotes *in situ* precipitation, consistent with the *in situ* heat treatment effects reported in literature (Schimbäck et al., 2024). Although the matrix supersaturation is expected to be locally reduced near the coarse Mg–Zn–Al-rich phase, the high dislocation density provides favourable nucleation sites (Aster et al., 2025; Samberger et al., 2023; Stemper et al., 2021).

3.8. Mechanical properties

3.8.1. Brinell hardness

To investigate the hardening potential two multi-step heat treatments HT1 and HT2 (see chapter 2.5) were applied. Both simulations were performed using the as-printed and homogenized materials .57 #7. The HT1 reached a maximum hardness of around 100 HBW after 4 h, after which the behaviour levelled off and showed signs of overaging rather than further strengthening. In the second treatment (HT2), the results show that while both treatments led to an initial increase in hardness over time, the HT2 condition provided better strengthening, reaching the highest measured value of 117 HBW after prolonged ageing of 110 h.

If the hardening responses of both alloys above are compared to wrought crossover alloy sheet material reported in the literature, the values are found to be significantly reduced. This is attributed to the lower Mg and Zn content retained after PBF-LB/M processing, which limits the achievable precipitation strengthening (Klein et al., 2023; Stemper et al., 2021), together with an early onset of failure. Significantly higher hardness and strength levels have also been reported for crossover alloys processed by WAAM, where solute losses are less pronounced and a higher Mg and Zn reservoir remains available for potential T-phase precipitation (Klein et al., 2023).

In addition, the thermodynamic calculations in Figure 2 with the reduced Mg and Zn contents predicted this trend, indicating that the hardness level achieved after HT2 represents the peak hardening condition attainable for the present chemistry. Direct characterization of the nanoscale ageing precipitates responsible for this hardening response by HR-STEM or APT is identified as a priority for future work.

3.8.2. Tensile testing

The printed tensile specimens were only subjected to HT2 resulting from the hardening experiments shown in Figure 8. The strategy was chosen because the simulations indicated the highest hardening potential under the given alloy conditions, particularly considering the reduced Mg and Zn content in the specimens

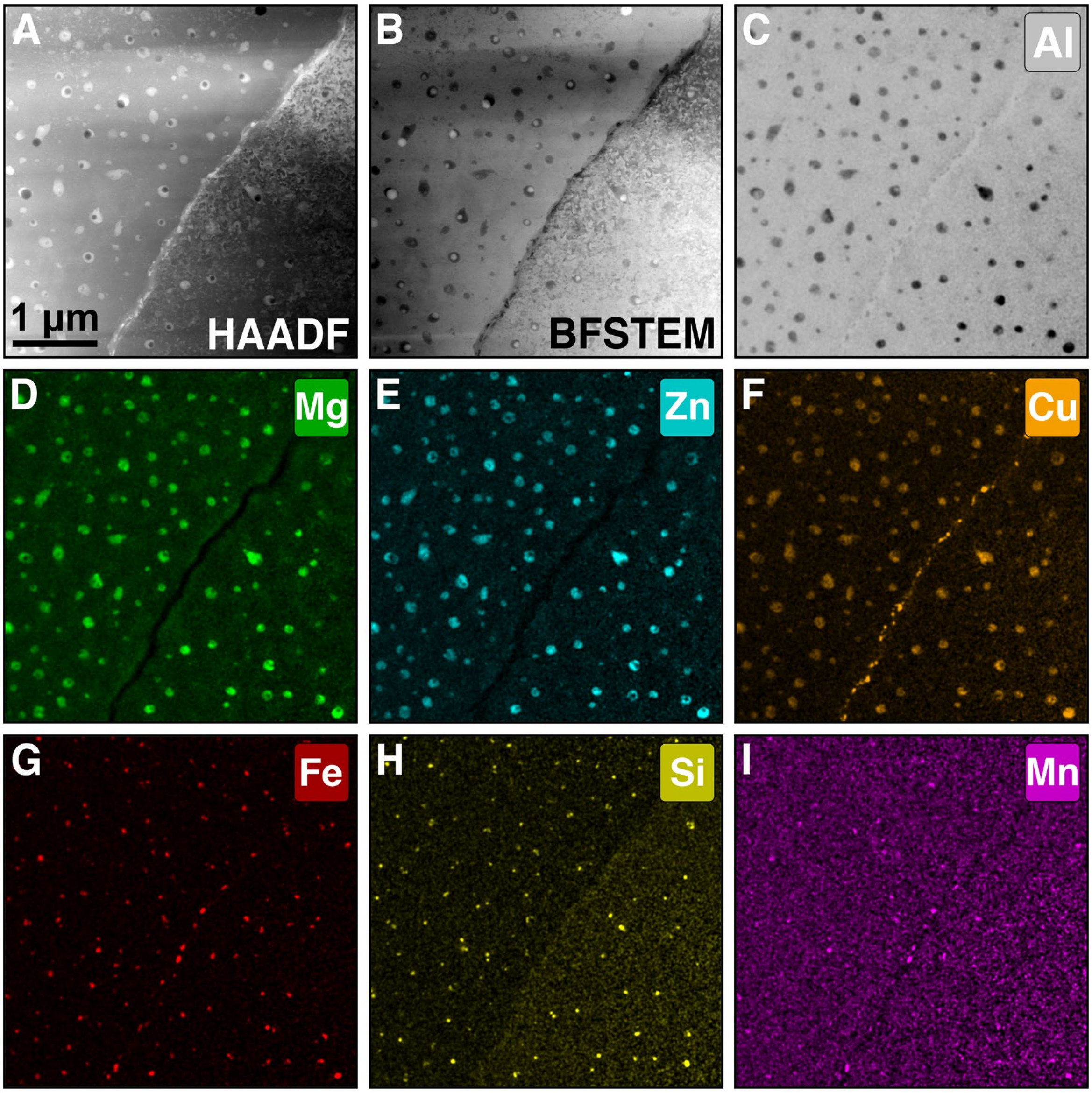

Figure 6. Mesoscale analytical characterization; STEM/EDX mapping of precipitates in the as-printed alloy; the scale bar of the HAADF image also applies for the EDX maps.

Table 3 summarizes the mechanical properties of the investigated alloys (.57 and .57 + Fe) in the as-printed and the heat-treated condition and compare it to a standard AlSi10Mg, to Scalmalloy®, to the alloy A20X and a high strength 7xxx series additive manufactured specimen (Gong et al., 2022; Kumar Ramavajjala et al., 2025; Saritha et al., 2025; Shaikh et al., 2023; Karimialavijeh et al. 2023).

Independently of the printing conditions and alloy modification, the crossover alloys exhibit in AM low tensile strength (180–230 MPa) and limited ductility (< 1%) in both conditions, with exclusively brittle fracture behaviour.

In contrast, AlSi10Mg, used as a benchmark alloy with excellent AM processability, shows significantly higher strength and ductility in both states, based on literature (Gong et al., 2022; Kumar Ramavajjala et al., 2025). The AM-processed 7050 alloy, show even lower strength (~100 MPa) and similar elongation (< 1%) in the as-printed condition compared to the crossover alloy. In contrast, the alloy exhibits a small increase in both tensile strength and ductility after heat treatment, indicating that strengthening mechanisms could become effective once solidification-related defects are mitigated (Saritha et al., 2025). A comparable trend is observed for Inconel 939, where crack sensitivity limits the as-printed performance, yet scan optimization and suitable heat

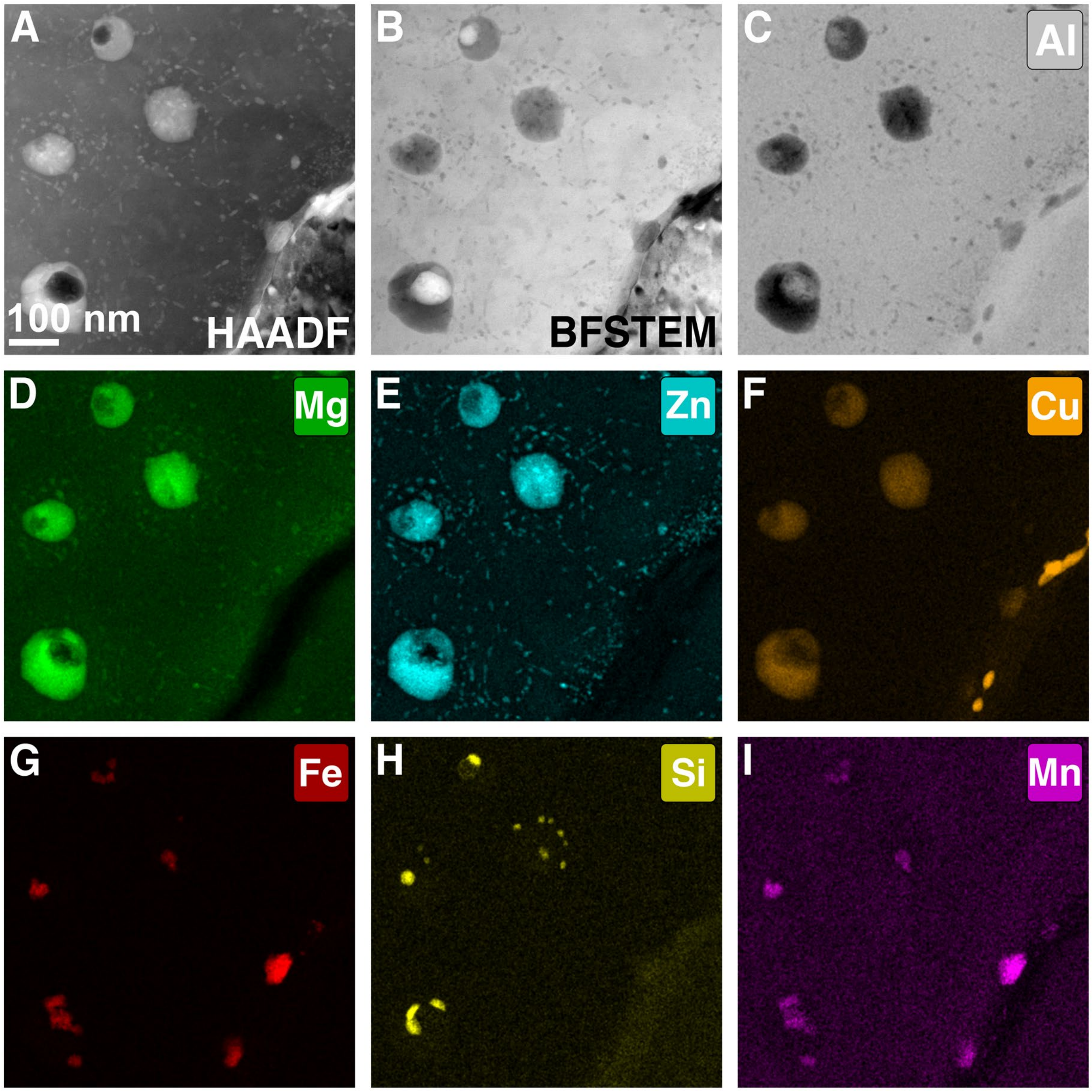

Figure 7. Nanoscale analytical characterization; STEM/EDX mapping of precipitates in the as-printed alloy; the scale bar of the HAADF image also applies for the EDX maps.

treatment result in high strength and a mixed ductile–brittle fracture at higher stress levels (Shaikh et al., 2023).

For the investigated alloys, the hardness increase after HT2 confirms precipitation strengthening consistent with thermodynamic predictions. However, this is not reflected in tensile properties like micro-cracks, lack of fusion and porosity dominate fracture initiation, masking heat-treatment-induced strengthening as observed in wrought crossover sheet material (Samberger et al., 2023; Stemper et al., 2021).

3.9. Fracture analysis

The fracture surfaces of the tensile specimens in the as-printed condition were analysed by scanning electron microscopy, as shown in Figure 9(A–D). No pronounced differences related to process parameters or alloy composition were observed, showing that fracture was primarily initiated by local microstructural failing e.g., pores and hot cracks, and processing-induced defects like lack of fusion.

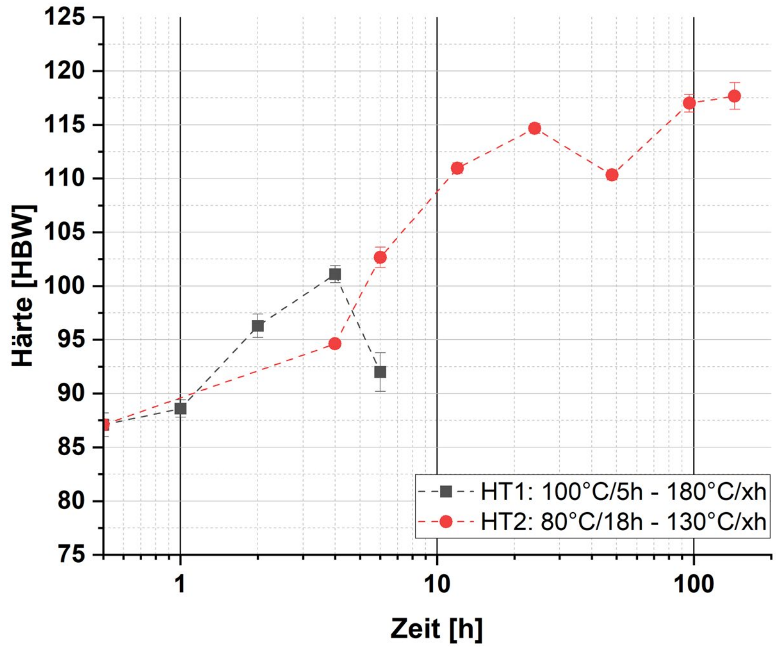

Figure 8. Hardening evolution during ageing on two different simulations (HT1 and HT2) on as printed samples. 57 #7.

Table 3. Mechanical properties of tensile strength and elongation for the printed samples in the as-printed and the heat-treated condition for the investigated alloy and, for comparison, three additional alloys.

Condition	Parameter	Alloy	Tensile strength R_m [N/mm^2]	Elongation at break A_{20} [%]
As-printed	#6	.57	183 ± 2	0.7 ± 0.0
HT 2	#6	.57	199 ± 2	0.2 ± 0.1
As-printed	#7	.57	189 ± 6	0.6 ± 0.1
HT 2	#7	.57	222 ± 4	0.2 ± 0.1
As-printed	#6	.57 + Fe	177 ± 16	0.5 ± 0.2
HT 2	#6	.57 + Fe	206 ± 34	0.3 ± 0.1
As-printed	#7	.57 + Fe	227 ± 15	0.6 ± 0.2
HT 2	#7	.57 + Fe	228 ± 10	0.3 ± 0.1
As-printed	(Gong et al., 2022)	AlSi10Mg	418 ± 14	5.4 ± 0.4
T6	(Kumar Ramavajjala et al., 2025)	AlSi10Mg	292 ± 4	3.9 ± 0.5
As-printed	(Cabrera-Correa et al., 2023)	Scalmalloy®	256 ± 4	~ 20
HT	(Cabrera-Correa et al., 2023)	Scalmalloy®	454 ± 3	~ 13
As-printed	(Saritha et al., 2025)	AM 7050 sample	101 ± 2	0.5 ± 0.0
2 step HT	(Saritha et al., 2025)	AM 7050 sample	230 ± 2	2.1 ± 0.0
As-printed	(Karimialavijeh et al., 2023)	A20X	289 ± 2	18 ± 0.8
T7	(Karimialavijeh et al., 2023)	A20X	370 ± 9	7.3 ± 0.3

Note: All samples are printed and tested vertically.

At lower magnification, the fracture surfaces show an irregular morphology with locally distributed cavities (Figure 9(B,D)), some of which contain partially unmelted powder particles (Figure 9(C)). These features indicate that lack-of-fusion defects contributed to crack initiation and premature failure, consistent with previous observations in additively manufactured aluminium alloys (Gudeljevic & Klein, 2021; Y. Wang et al., 2021). The irregular cavity morphology further suggests insufficient local melt pool consolidation rather than gas porosity (Y. Wang et al., 2021).

Higher-magnification images reveal fracture features dominated by lamellar and faceted regions, indicating a predominantly brittle fracture with limited plastic deformation (Gudeljevic & Klein, 2021; J. H. Martin et al., 2017).

3.10. Future design strategies for AM-tailored crossover alloys

Al–Mg–Zn–(Cu) crossover aluminium alloys have been shown to be difficult to process by Powder Bed Fusion – Laser Beam/Metal. Although there is one previous study showing promising WAAM

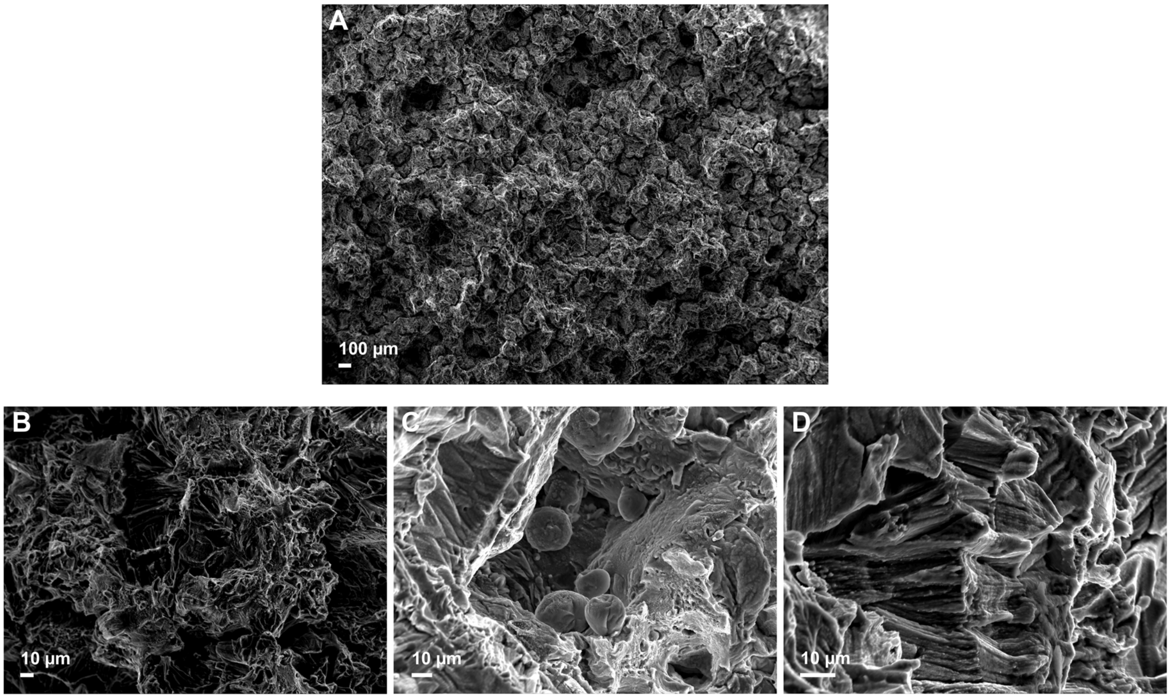

Figure 9. Overview of fracture surface analysis with SEM on the sample. 57 #7 (a), higher resolution of the crack surface after tensile testing (B), unmelted powder particles in cavities (C) and a lamellar structure that indicates a brittle fracture (D).

results (Klein et al., 2021), these alloys suffer from porosity, hot cracking, columnar grain growth, and limited precipitation response due to evaporation of Mg and Zn. For the potential application of crossover alloy in AM (i.e., for repair in space) the powder base alloy needs further development.

Grain-structure control is critical, with strategies that promote equiaxed growth and high growth restriction to reduce crack-driving anisotropy. Micro-alloying with Sc + Zr was reported particularly effective, as Al_3(Sc,Zr) dispersoids enable grain refinement, crack resistance, and thermal stability (Schimbäck et al., 2022; Spierings et al., 2017; Xu et al., 2023). Grain refiners such as TiB_2 or TiC nanoparticles could further assist heterogeneous nucleation (J. H. Martin et al., 2017), but their effect depends strongly on spatial dispersion and may be considered complementary.

Mg and Zn evaporation must be anticipated by chemistries that tolerate solute loss while retaining precipitation potential. Together with this adaptation, control of the solidification path through benign terminal reactions and sufficient interdendritic feeding should be examined. While adapting the chemical composition for potential evaporation effects, one could also aim to minimize the terminal freezing range (e.g., via thermochemical simulations; Kou, 2003) to reduce hot cracking susceptibility (Saritha et al., 2025; Schimbäck et al., 2022; Stopyra et al., 2020).

In summary, the analysis suggests that integrated alloy–process co-design is necessary for the alloy, rather than simply applying wrought aluminium chemistries. Consequently, the compatibility of the base crossover materials must also be tested and optimized.

4. Conclusion

The present study established processing-microstructure-property relationships for an Al–Mg–Zn–(Cu) crossover alloy processed by PBF-LB/M. A stable process window was identified at VED 70 J/mm^3 and LED 0.125–0.150 J/mm, yielding relative densities above 98.5%. However, significant Mg and Zn evaporation occurred during processing, increasing the Mg/Zn ratio and reducing the available solute content for precipitation hardening.

Electron microscopy revealed a pronounced columnar grain structure and the formation of coarse Mg–Zn–Al–(Cu)-rich precipitates in the as-printed state, despite thermodynamic predictions indicating limited equilibrium stability.

Mechanical testing showed limited strength (180–230 MPa) and negligible ductility (<1%), independent of heat treatment. The restricted hardening response is attributed to solidification-induced defects acting as dominant crack initiation sites.

The results demonstrate that direct transfer of wrought crossover chemistries to PBF-LB/M is currently insufficient for structural or repair use. Integrated alloy-process co-design strategies accounting for evaporation, crack susceptibility, and grain structure control are required before crossover alloys can realize their potential in additive manufacturing applications.

Acknowledgments

The work of I.W., and S.S. was funded by the Christian Doppler Research Association within the framework of the Christian Doppler Laboratory for Deformation-Precipitation Interactions in Aluminium Alloys (I.W.) and the Christian Doppler Laboratory for Advanced Aluminium Alloys (S.P.). The financial support received from the Austrian Federal Ministry of Labour and Economy, the National Foundation for Research, Technology and Development and the Christian Doppler Research Association. The research reported on here was supported by the Austrian Research Promotion Agency (FFG) in the context of projects 3DnanoAnalytics (FFG-No. 858040). Additionally, the authors received the support from AMAG rolling AG and the Industrial and Materials Science department at the Chalmers University of Technology.

Author contributions

CRediT: **Andreas Weidinger**: Conceptualization, Data curation, Formal analysis, Investigation, Methodology, Project administration, Validation, Visualization, Writing – original draft, Writing – review & editing; **Dmitri Riabov**: Investigation, Methodology, Resources, Supervision, Writing – review & editing; **Sebastian Samberger**: Data curation, Methodology, Validation, Visualization, Writing – review & editing; **Phillip Dumitraschkewitz**: Conceptualization, Data curation, Resources, Software, Writing – review & editing; **Irmgard Weißensteiner**: Conceptualization, Validation, Writing – review & editing; **Florian. Schmid**: Methodology, Resources, Supervision, Validation, Writing – review & editing; **Lukas Stemper**: Investigation, Resources, Supervision, Writing – review & editing; **Matheus A. Tunes**: Conceptualization, Data curation, Investigation, Methodology, Resources, Supervision, Validation, Visualization, Writing – review & editing; **Lars Nyborg**: Project administration, Resources, Supervision, Writing – review & editing; **Stefan Pogatscher**: Conceptualization, Formal analysis, Funding acquisition, Project administration, Resources, Supervision, Validation, Writing – review & editing.

Declaration of generative AI and AI-assisted technologies in the writing process

During the preparation of this work the author used ChatGPT and DeepL Write in order to improve readability and language of this work. After using these tools, the author reviewed and edited the content as needed and take full responsibility for the content of the publication.

Disclosure statement

No potential conflict of interest was reported by the author(s).

Notes on contributors

Andreas Weidinger is a PhD candidate at the Chair of Nonferrous Metallurgy at Montanuniversität Leoben, where he works within the Christian Doppler Laboratory for Advanced Aluminum Alloys. His research covers the continuous casting of established and novel aluminium alloys, with a particular focus on the additive manufacturing of newly developed alloy systems.

Dmitri Riabov received his PhD from the Department of Industrial and Materials Science at Chalmers University of Technology in 2022 with a thesis on laser-based powder bed fusion of stainless steels. His expertise lies in the relationship between powder characteristics, process parameters and the resulting properties of additively manufactured metals.

Sebastian Samberger completed his PhD at the Chair of Nonferrous Metallurgy at Montanuniversität Leoben on the optimisation and industrial establishment of aluminium crossover alloys. As a postdoctoral researcher he subsequently spent six months on a research stay at the Tokyo Institute of Technology in Tokyo, Japan. His work addresses the industrial processing of these alloys and the influence of impurities introduced by recycled feedstock.

Phillip Dumitraschkewitz earned his doctorate at the Chair of Nonferrous Metallurgy at Montanuniversität Leoben, where he studied clustering and diffusion in aluminium alloys during natural ageing. He combines atom probe tomography and transmission electron microscopy with calorimetric methods and has several years of experience in the nanoscale characterisation of precipitation phenomena.

Irmgard Weißensteiner completed her PhD in materials science at Montanuniversität Leoben. She heads a Christian Doppler Laboratory at the Chair of Nonferrous Metallurgy, where her group investigates deformation–precipitation interactions in aluminium alloys with a high recycled content for aerospace and transport applications.

Florian Schmid completed his PhD at Montanuniversität Leoben on the ageing behaviour of Al–Mg–Si alloys. He has since gained several years of industrial experience in aluminium alloy development, focusing on the transfer of research results into industrial practice.

Lukas Stemper completed his PhD at Montanuniversität Leoben on the potential of aluminium crossover alloys. He works as a research and development engineer in product and process development at AMAG Austria Metall AG, where he focuses on bringing new alloy concepts into industrial production.

Prof. Matheus A. Tunes, BSc MSc PhD MInstP – Assistant Professor, Chair of Nonferrous Metallurgy, Montanuniversität Leoben (since 2023), where he founded the [X-MAT] laboratory, dedicated to the development, characterisation and testing of materials for extreme environments. He is also an Visiting Fellow at UKAEA. BSc Physics and MSc Materials Science, University of São Paulo, Brazil; PhD at the MIAMI Facilities, University of Huddersfield, United Kingdom, on atomic collisions in solids and electron microscopy. An expert in materials design, his research spans hydrogen energy materials, thermonuclear fusion, corrosion, advanced fuel cells, high-temperature materials for hypersonic flight, and new materials.

Lars Nyborg is a full professor at the Division of Materials and Manufacture, Department of Industrial and Materials Science, Chalmers University of Technology, and has served as Director of the Chalmers Production Area of Advance. He received his doctorate from the same university and has spent his career at Chalmers, where he has authored or co-authored more than 300 scientific publications. His research focuses on surface engineering and the surface chemistry of metal powders, powder metallurgy, and the additive manufacturing of steels, aluminium alloys and other advanced materials.

Stefan Pogatscher is a full professor of "Metallurgy of Sustainable Light Metal Alloys" and Head of the Department Metallurgy at Montanuniversität Leoben. He received his doctorate from the same university in 2012 and worked as a postdoc at ETH Zurich from 2012 to 2015 before returning to Leoben. His research focuses on the metallurgy of sustainable light metals, circular alloy design, and high-resolution materials characterization.

Data availability statement

The raw material and processed data required to reproduce these findings can be shared at this time, upon request.

References

Aegerter, J., Kühn, H.-J., Frenz, H., & Weißmüller, C. (2011). DIN EN ISO 6892-1: 2009 The tensile test—initial findings from the practical implementation of the new standard. *Materials Testing*, *53*(10), 586–594. https://doi.org/10.3139/120.110268

Aster, P., Dumitraschkewitz, P., Uggowitzer, P. J., Weißensteiner, I., Tunes, M. A., Schmid, F., Stemper, L., & Pogatscher, S. (2025). Effect of long-term aging and Cu addition on clustering, strength and strain hardening in Al-Mg-Zn-(Cu) crossover alloys. *Materials and Design*, *257*, 114341. https://doi.org/10.1016/j.matdes.2025.114341

ASTM International. (2019). Standard practice for determining average grain size using electron backscatter diffraction (EBSD) in fully recrystallized polycrystalline materials (E2627-13). West Conshohocken, PA: ASTM International.

ASTM International. (2017). Standard test method for analysis of aluminum and aluminum alloys by inductively coupled plasma atomic emission spectrometry performance based method (E3061-17). West Conshohocken, PA: ASTM International.

Babu, A., Kairy, S. K., Huang, A., & Birbilis, N. (2020). Laser powder bed fusion of high solute Al-Zn-Mg alloys: Processing, characterisation and properties. *Materials and Design*, *196*, 109183. https://doi.org/10.1016/j.matdes.2020.109183

Bale, C. W., Chartrand, P., Degterov, S. A., Eriksson, G., Hack, K., Ben Mahfoud, R., Melançon, J., Pelton, A. D., & Petersen, S. (2002). FactSage thermochemical software and databases. *Calphad - Computer Coupling of Phase Diagrams and Thermochemistry*, *26*(2), 189–228. https://doi.org/10.1016/S0364-5916(02)00035-4

Beevers, E., Mena, N. J., Thijs, L., Nutal, N., Norman, A., & Van Hooreweder, B. (2024). Development of a 7000 series aluminium alloy suitable for laser-based additive manufacturing. *Materials Science and Engineering: A*, *916*, 147334. https://doi.org/10.1016/j.msea.2024.147334

Cabrera-Correa, L., González-Rovira, L., de Dios López-Castro, J., Castillo-Rodríguez, M., & Botana, F. J. (2023). Effect of the heat treatment on the mechanical properties and microstructure of Scalmalloy® manufactured by selective laser melting (SLM) under certified conditions. *Materials Characterization*, *196*, 112549. https://doi.org/10.1016/j.matchar.2022.112549

Cao, C., Zhang, D., Zhuang, L., & Zhang, J. (2017). Improved age-hardening response and altered precipitation behavior of Al-5.2 Mg-0.45 Cu-2.0 Zn (wt%) alloy with pre-aging treatment. *Journal of Alloys and Compounds*, *691*, 40–43. https://doi.org/10.1016/j.jallcom.2016.08.206

Casati, R., Coduri, M., Riccio, M., Rizzi, A., & Vedani, M. (2019). Development of a high strength Al–Zn–Si–Mg–Cu alloy for selective laser melting. *Journal of Alloys and Compounds*, *801*, 243–253. https://doi.org/10.1016/j.jallcom.2019.06.123

Chen, Q., Zhao, Y., Strayer, S., Zhao, Y., Aoyagi, K., Koizumi, Y., Chiba, A., Xiong, W., & To, A. C. (2021). Elucidating the effect of preheating temperature on melt pool morphology variation in Inconel 718 laser powder bed fusion via simulation and experiment. *Additive Manufacturing*, *37*, 101642. https://doi.org/10.1016/j.addma.2020.101642

DebRoy, T., Wei, H. L., Zuback, J. S., Mukherjee, T., Elmer, J. W., Milewski, J. O., Beese, A. M., Wilson-Heid, A., De, A., & Zhang, W. (2018). Additive manufacturing of metallic components–process, structure and properties. *Progress in Materials Science*, *92*, 112–224. https://doi.org/10.1016/j.pmatsci.2017.10.001

Ebenberger, P., Uggowitzer, P. J., Kirnstötter, S., Gerold, B., Zaefferer, S., & Pogatscher, S. (2019). Processing-controlled suppression of Lüders elongation in AlMgMn alloys. *Scripta Materialia*, *166*, 64–67. https://doi.org/10.1016/j.scriptamat.2019.02.047

Fardan, A., Fazi, A., Peng, R. L., Mishurova, T., Thuvander, M., Bruno, G., Brodin, H., & Hryha, E. (2024). Fine-tuning melt pools and microstructures: Taming cracks in powder bed fusion—Laser beam of a non-weldable Ni-base superalloy. *Materialia*, *34*, 102059. https://doi.org/10.1016/j.mtla.2024.102059

Ferro, P., Meneghello, R., Savio, G., & Berto, F. (2020). A modified volumetric energy density–based approach for porosity assessment in additive manufacturing process design. *The International Journal of Advanced Manufacturing Technology*, *110*(7-8), 1911–1921. https://doi.org/10.1007/s00170-020-05949-9

Gong, J., Wei, K., Liu, M., Song, W., Li, X., & Zeng, X. (2022). Microstructure and mechanical properties of AlSi10Mg alloy built by laser powder bed fusion/direct energy deposition hybrid laser additive manufacturing. *Additive Manufacturing*, *59*, 103160. https://doi.org/10.1016/j.addma.2022.103160

Gudeljevic, M., & Klein, T. (2021). Investigation of material characteristics of intersections built by wire and arc additive manufacturing using locally varying deposition parameters. *The International Journal of Advanced Manufacturing Technology*, *116*(5-6), 2021–2029. https://doi.org/10.1007/s00170-021-07548-8

Herzog, D., Seyda, V., Wycisk, E., & Emmelmann, C. (2016). Additive manufacturing of metals. *Acta Materialia*, *117*, 371–392. https://doi.org/10.1016/j.actamat.2016.07.019

Hoffmann, M., & Elwany, A. (2023). In-space additive manufacturing: A review. *Journal of Manufacturing Science and Engineering*, *145*(2), 020801. https://doi.org/10.1115/1.4055603

Karimialavijeh, H., Ghasri-Khouzani, M., Chakraborty, A., Pröbstle, M., & Martin, É. (2023). Direct aging of additively manufactured A20X aluminum alloy. *Journal of Alloys and Compounds*, *968*, 172071. https://doi.org/10.1016/j.jallcom.2023.172071

Klein, T., Arnoldt, A., Gomes, M., & Barriobero-Vila, P. (2023). Microstructure and mechanical properties of an advanced Ag-microalloyed aluminum crossover alloy tailored for wire-arc directed energy deposition. *JOM Journal of the Minerals Metals and Materials Society*, *75*(10), 4128–4137. https://doi.org/10.1007/s11837-023-05838-y

Klein, T., Graf, G., Staron, P., Stark, A., Clemens, H., & Spoerk-Erdely, P. (2021). Microstructure evolution induced by the intrinsic heat treatment occurring during wire-arc additive manufacturing of an Al-Mg-Zn-Cu crossover alloy. *Materials Letters*, *303*, 130500. https://doi.org/10.1016/j.matlet.2021.130500

Knacke, O., & Stranski, I. (1956). The mechanism of evaporation. *Progress in Metal Physics*, *6*, 181–235. https://doi.org/10.1016/0502-8205(56)90007-7

Kou, S. (2003). Welding metallurgy. second ed., John Wiley & Sons, Inc., New Jersey, *431*, 223–225

Kumar Ramavajjala, A., Dandekar, T. R., Khatirkar, R. K., Joshi, C., Chouhan, R. N., & Agnihotri, A. (2025). A review on the correlation between microstructure, heat treatment and mechanical properties of additively manufactured AlSi10Mg by LPBF. *Critical Reviews in Solid State Material Science*, *50*(3), 239–274. https://doi.org/10.1080/10408436.2024.2414012

Mair, P., Kaserer, L., Braun, J., Stajkovic, J., Klein, C., Schimbäck, D., Perfler, L., Zhuravlev, E., Kessler, O., & Leichtfried, G. (2022). Dependence of mechanical properties and microstructure on solidification onset temperature for Al2024–CaB6 alloys processed using laser powder bed fusion. *Materials Science and Engineering: A*, *833*, 142552. https://doi.org/10.1016/j.msea.2021.142552

Martin, J. H., Yahata, B. D., Hundley, J. M., Mayer, J. A., Schaedler, T. A., & Pollock, T. M. (2017). 3D printing of high-strength aluminium alloys. *Nature*, *549*(7672), 365–369. https://doi.org/10.1038/nature23894

Murr, L. E. (2018). A metallographic review of 3D printing/additive manufacturing of metal and alloy products and components. *Metallography, Microstructure, and Analysis*, *7*(2), 103–132. https://doi.org/10.1007/s13632-018-0433-6

Nesmeyanov, A. N. (1963). *Vapor pressure of the chemical elements*. Elsevier.

Oxford Instruments Nano Analysis. (2022). *AZtec EBSD data analysis user guide*. UK: High Wycombe.

Qin, H., Dong, Q., Fallah, V., & Daymond, M. R. (2020). Rapid solidification and non-equilibrium phase constitution in laser powder bed fusion (LPBF) of AlSi10Mg alloy: Analysis of nano-precipitates, eutectic phases, and hardness evolution. *Metallurgical and Materials Transactions A*, *51*(1), 448–466. https://doi.org/10.1007/s11661-019-05505-5

Rometsch, P. A., Zhu, Y., Wu, X., & Huang, A. (2022). Review of high-strength aluminium alloys for additive manufacturing by laser powder bed fusion. *Materials and Design*, *219*, 110779. https://doi.org/10.1016/j.matdes.2022.110779

Samberger, S., Weißensteiner, I., Stemper, L., Kainz, C., Uggowitzer, P. J., & Pogatscher, S. (2023). Fine-grained aluminium crossover alloy for high-temperature sheet forming. *Acta Materialia*, *253*, 118952. https://doi.org/10.1016/j.actamat.2023.118952

Saritha, L., Jeyaprakash, N., Ariga, T. S., Vijayakumar, P., Shankar, K. V., Manoj, M., & Govind, A. (2025). Investigation of the impact of T6 and direct aging heat treatment on the microstructure and mechanical behaviour of additively manufactured AA7075 alloy. *Results in Engineering*, *28*, 107521. https://doi.org/10.1016/j.rineng.2025.107521

Schimbäck, D., Kaserer, L., Mair, P., Mohebbi, M. S., Staron, P., Maier-Kiener, V., Letofsky-Papst, I., Kremmer, T., Palm, F., Montes, I., Höppel, H. W., Leichtfried, G., & Pogatscher, S. (2024). Advancements in metal additive manufacturing: In-situ heat treatment of aluminium alloys during the laser powder bed fusion process. *Materials Science and Engineering: A*, *905*, 146102. https://doi.org/10.1016/j.msea.2024.146102

Schimbäck, D., Mair, P., Bärtl, M., Palm, F., Leichtfried, G., Mayer, S., Uggowitzer, P. J., & Pogatscher, S. (2022). Alloy design strategy for microstructural-tailored scandium-modified aluminium alloys for additive manufacturing. *Scripta Materialia*, *207*, 114277. https://doi.org/10.1016/j.scriptamat.2021.114277

Shaikh, A. S., Rashidi, M., Minet-Lallemand, K., & Hryha, E. (2023). On as-built microstructure and necessity of solution treatment in additively manufactured Inconel 939. *Powder Metallurgy*, *66*(1), 3–11. https://doi.org/10.1080/00325899.2022.2041787

Spierings, A. B., Dawson, K., Heeling, T., Uggowitzer, P. J., Schäublin, R., Palm, F., & Wegener, K. (2017). Microstructural features of Sc-and Zr-modified Al-Mg alloys processed by selective laser melting. *Materials and Design*, *115*, 52–63. https://doi.org/10.1016/j.matdes.2016.11.040

Stemper, L., Tunes, M. A., Dumitraschkewitz, P., Mendez-Martin, F., Tosone, R., Marchand, D., Curtin, W. A., Uggowitzer, P. J., & Pogatscher, S. (2021). Giant hardening response in AlMgZn(Cu) alloys. *Acta Materialia*, *206*, 116617. https://doi.org/10.1016/j.actamat.2020.116617

Stemper, L., Tunes, M. A., Tosone, R., Uggowitzer, P. J., & Pogatscher, S. (2022). On the potential of aluminum crossover alloys. *Progress in Materials Science*, *124*, 100873. https://doi.org/10.1016/j.pmatsci.2021.100873

Stopyra, W., Gruber, K., Smolina, I., Kurzynowski, T., & Kuźnicka, B. (2020). Laser powder bed fusion of AA7075 alloy: Influence of process parameters on porosity and hot cracking. *Additive Manufacturing*, *35*, 101270. https://doi.org/10.1016/j.addma.2020.101270

Tunes, M. A. (2026). The legacy and future of aluminum alloys: Space exploration and extraterrestrial settlement. *ACS Materials Au*, *6*(1), 1–27. https://doi.org/10.1021/acsmaterialsau.5c00139

Tunes, M. A., Stemper, L., Greaves, G., Uggowitzer, P. J., & Pogatscher, S. (2020). Prototypic lightweight alloy design for stellar-radiation environments. *Advanced Science*, *7*(22), 2002397. https://doi.org/10.1002/advs.202002397

Vander Voort, G. F. (1999). *Metallography, principles and practice*. ASM International.

Wang, T., Wang, Y., Yang, X., Chen, B., & Zhu, H. (2022). Cracks and process control in laser powder bed fusion of Al-Zn-Mg alloy. *Journal of Manufacturing Processes*, *81*, 571–579. https://doi.org/10.1016/j.jmapro.2022.06.066

Wang, Y., Wu, X., Cao, L., Tong, X., Zou, Y., Zhu, Q., Tang, S., Song, H., & Guo, M. (2021). Effect of Ag on aging precipitation behavior and mechanical properties of aluminum alloy 7075. *Materials Science and Engineering: A*, *804*, 140515. https://doi.org/10.1016/j.msea.2020.140515

Weidinger, A., Riabov, S., Samberger, S., Dumitraschkewitz, P., Stemper, L., Schmid, F., Neuberte, S., Nyborg, L., & Pogatscher, S. (2025). Exploring the feasibility of 5/7-crossover alloy in AM, process evaluation, porosity and element loss. In *EMC 2025 Proceeding*.

Willenshofer, P. D., Tunes, M. A., Kainz, C., Renk, O., Kremmer, T. M., Gneiger, S., Uggowitzer, P. J., & Pogatscher, S. (2023). Precipitation behaviour in AlMgZnCuAg crossover alloy with coarse and ultrafine grains. *Materials Research Letters*, *11*(12), 1063–1072. https://doi.org/10.1080/21663831.2023.2281589

Willenshofer, P. D., Tunes, M. A., Vo, H. T., Stemper, L., Alfreider, M., Renk, O., Greaves, G., Kiener, D., Uggowitzer, P. J., & Pogatscher, S. (2026). Radiation-resistant aluminum alloy for space missions in the extreme environment of the solar system. *Advanced Materials*, *38*(20), e13450. https://doi.org/10.1002/adma.202513450

Xu, J.-Y., Zhang, C., Liu, L.-X., Guo, R., Sun, M.-J., & Liu, L. (2023). Achieving high strength in laser powder-bed fusion processed AlFeCuZr alloy via dual-nanoprecipitations and grain boundary segregation. *Journal of Materials Science and Technology*, *137*, 56–66. https://doi.org/10.1016/j.jmst.2022.07.033

Yoshioka, J., & Eshraghi, M. (2023). Temporal evolution of temperature gradient and solidification rate in laser powder bed fusion additive manufacturing. *Heat and Mass Transfer*, *59*(7), 1155–1166. https://doi.org/10.1007/s00231-022-03318-8

Zhou, L., Hyer, H., Thapliyal, S., Mishra, R. S., McWilliams, B., Cho, K., & Sohn, Y. (2020). Process-dependent composition, microstructure, and printability of Al-Zn-Mg and Al-Zn-Mg-Sc-Zr alloys manufactured by laser powder bed fusion. *Metallurgical and Materials Transactions A*, *51*(6), 3215–3227. https://doi.org/10.1007/s11661-020-05768-3

Appendix

The following Table A1 gives an overview of all printed parameter variations during the DOE of this study. The samples were produced as cubes with an edge length of 10 × 10 × 10 mm.

Table A1. Overview of the 55 parameters studied during the DOE.

Set	Power [W]	Layer [µm]	Temp. [°C]	Speed [mm/s]	Hatch [mm]	VED [J/mm^3]	LED [J/mm]
#1	370	30	110	1600	0.05	154	0.23
#2	370	30	110	1600	0.085	91	0.23
#3	370	30	110	1300	0.12	79	0.29
#4	370	30	110	800	0.155	99	0.46
#5	370	30	110	800	0.19	81	0.46
#6	370	30	110	2400	0.05	103	0.15
#7	370	30	110	1500	0.085	97	0.25
#8	370	30	110	1000	0.12	103	0.37
#9	370	30	110	1000	0.155	80	0.37
#10	370	30	110	1000	0.19	65	0.37
#11	370	30	110	2500	0.05	99	0.15
#12	370	30	110	1200	0.085	121	0.31
#13	370	30	110	1200	0.12	86	0.31
#14	370	30	110	1200	0.155	66	0.31
#15	370	30	110	1200	0.19	54	0.31
#16	370	30	110	2600	0.05	95	0.14
#17	370	30	110	1400	0.085	104	0.26
#18	370	30	110	1400	0.12	73	0.26
#19	370	30	110	1400	0.155	57	0.26
#20	370	30	110	1400	0.19	46	0.26
#21	300	30	110	1400	0.07	102	0.21
#22	300	30	110	1400	0.1	71	0.21
#23	300	30	110	1500	0.07	95	0.20
#24	300	30	110	1500	0.1	67	0.20
#25	320	30	110	1400	0.07	109	0.23
#26	320	30	110	1400	0.1	76	0.23
#27	320	30	110	1500	0.07	102	0.21
#28	320	30	110	1500	0.1	71	0.21
#29	335	30	110	1400	0.07	114	0.24
#30	335	30	110	1400	0.1	80	0.24
#31	335	30	110	1500	0.07	106	0.22
#32	335	30	110	1500	0.1	74	0.22
#33	350	30	110	1400	0.07	119	0.25
#34	350	30	110	1400	0.1	83	0.25
#35	370	30	110	2600	0.05	95	0.14
#36	370	30	110	2500	0.05	99	0.15
#37	370	30	110	2400	0.05	103	0.15
#38	370	30	110	1600	0.05	154	0.23
#39	370	30	110	1600	0.085	91	0.23
#40	370	30	110	1500	0.085	97	0.25
#41	370	30	110	1400	0.085	104	0.26
#42	370	30	110	1400	0.12	73	0.26
#43	370	30	110	1400	0.155	57	0.26
#44	370	30	110	1400	0.19	46	0.26
#45	370	30	110	1300	0.12	79	0.28
#46	370	30	110	1200	0.085	121	0.31
#47	370	30	110	1200	0.12	86	0.31
#48	370	30	110	1200	0.155	66	0.31
#49	370	30	110	1200	0.19	54	0.31
#50	370	30	110	1000	0.12	103	0.37
#51	370	30	110	1000	0.155	80	0.37
#52	370	30	110	1000	0.19	65	0.37
#53	370	30	110	800	0.155	99	0.46
#54	370	30	110	800	0.19	81	0.46
#55	370	30	110	2600	0.05	95	0.14